

Research Article



## Implementation of Multitemporal Synthetic Aperture Radar for Ground Hazard Risk Monitoring on Railway Right of Way

Transportation Research Record I-23
© The Author(s) 2025
© ① ③
Article reuse guidelines:

sagepub.com/journals-permissions DOI: 10.1177/03611981251372086 journals.sagepub.com/home/trr



Dimitris C. Rizos<sup>I</sup>, Sumanth Varma Byrraju<sup>I</sup>, Michael A. Sutton<sup>2</sup>, and Ning Li<sup>2†</sup>

#### **Abstract**

Railway transportation has been the backbone of national economies worldwide. When geohazards occur and damage the network, they affect railway operations, resulting in delays and detrimental social and economic effects. A potential tool for monitoring the vast network for geohazards is satellite-based radars. Interferometric synthetic aperture radar (InSAR) may be used to study a wide range of geophysical phenomena. Its ability to study geohazards is frequently constrained by several challenges stemming from adverse atmospheric effects and wave scattering associated with site conditions and terrain characteristics. The authors have developed the framework of a monitoring system that uses satellite radar imagery analysis for identifying geohazard-prone locations through continuous monitoring of large regions. This paper discusses one implementation of multitemporal InSAR techniques that includes the new concept of a "Rolling SAR Image Stack." In addition, it introduces three postprocessing techniques that enable the detection of critical locations where geohazard failures may initiate along the railway right of way before an event takes place. A site characterization and classification guide is introduced to facilitate the selection of the most effective SAR analysis method for monitoring the area of interest. The guide considers on-site conditions affecting the quality and availability of radar data. This paper summarizes the investigations, methodologies, and approaches that led to the development of the workflow of the proposed monitoring system and demonstrates the ability of the proposed monitoring framework to identify critical locations of geohazard failure potential through implementation case studies.

#### **Keywords**

geohazard, failure initiation, geohazard monitoring, MTInSAR, remote sensing

Railway transportation has been the backbone of national economies worldwide, facilitating strong commercial connections, and enabling efficient transit. Its benefits over other modes of transportation are well established and include a large carrying capacity, low operating costs, extensive range, smaller carbon footprint, and weather resilience (1). Railroads frequently travel over rugged terrain and often traverse natural or constructed slopes susceptible to shallow geohazards such as landslides and subsidence (2). Geohazards are critical geologic conditions with a high potential to cause significant damage to infrastructure, property, and even loss of life. Shallow geohazards occur in the upper layer

of the Earth's crust and have a direct impact on infrastructure (3). Geohazards progress slowly over long periods of time, and they are relatively stable until triggered by external events such as rainfall, mining, and construction (4). Geohazard failures when they occur along the

#### **Corresponding Author:**

Dimitris C. Rizos, rizos@engr.sc.edu

<sup>&</sup>lt;sup>1</sup>Department of Civil and Environmental Engineering, University of South Carolina, Columbia, SC

<sup>&</sup>lt;sup>2</sup>Department of Mechanical Engineering, University of South Carolina, Columbia, SC

<sup>†</sup>Deceased

railway right of way (ROW) cause significant damage to railway infrastructure and affect railway safety and operations, resulting in service disruption and potentially detrimental social and economic effects (5). The early detection of shallow geohazards is critical to safety and to maintain the network in a state of good repair. Detection relies on identifying and monitoring their underlying causes (6-11).

Satellite-based radars have gained popularity as innovative tools for monitoring the vast railway network for geohazards to significantly improve early warning and mitigation strategies (12). An imaging radar sensor on an orbiting satellite observing Earth's surface emits electromagnetic microwave beams (wavelength in the range 1 mm to 1 m) toward a target on the Earth's surface and captures the properties of the backscatter signal. The captured image contains information about the backscatter strength and the time delay between the incident and backscatter wave, is typically of very limited resolution, and depends primarily on the characteristics and properties of the target on the Earth's surface. Synthetic aperture radar (SAR) is a technique that synthesizes SAR images to produce much higher resolution images of vast areas (up to 250 km wide swaths) (13). Comparing the time delay (phase) information between any two SAR images obtained at different times allows detection of ground movement with respect to the satellite position, a process that creates an interferometric SAR (InSAR) image. InSAR has shown potential to investigate various geohazards, such as seismic cycles of earthquakes (14), volcanic activities (15), and slope failures (16). InSAR has been commonly employed for the mapping and monitoring of landslides globally (17, 18). While conventional InSAR may be used to study a wide range of geophysical phenomena, its ability to study geohazards is frequently constrained by several challenges stemming from phase decorrelation, and errors in phase unwrapping as a result of adverse atmospheric effects and wave scattering associated with site conditions and terrain characteristics. Limitations in conventional InSAR techniques have spurred the development of the multitemporal InSAR (MTInSAR) techniques. The MTInSAR techniques reduce errors in the displacement measurements and enable tracking changes over time. This is achieved by utilizing collections of InSAR images (interferograms) derived from an extensive series of SAR images (data stack) of the specific region under investigation (19). Although no single technique can solve all SAR limitations, selecting the appropriate technique based on limcan increase the efficiency of implementations in recognizing geohazards (20). Despite the advances of the MTInSAR techniques, their application for detecting landslides and other shallow geohazards is limited to mapping and monitoring the geohazards after their occurrence.

The authors have developed the framework of a remote monitoring system that utilizes satellite data and other data sources for the identification and localization of critical areas along the railway ROW that exhibit higher risk for geohazard failure initiation (21, 22). This is achieved by monitoring two main precursors to event initiation, that is, localized ground surface mobilization before the event initiation, and large, localized changes in soil moisture content (21). The InSAR family of signal processing is implemented for the monitoring of the sites. Changes of amplitude and phase of the signals between image acquisitions are correlated to changes in surface deformations, precipitation, and soil moisture content. The research team adapted three MTInSAR techniques, that is, persistent scatterer InSAR (PSInSAR), small baseline subset (SBAS), and coherence change detection (CCD), to improve the detection of scatterers in the broader region of interest by introducing the new concept of a "Rolling SAR Image Stack." Furthermore, the team developed three postprocessing is, Thresholding, techniques, that Scatterer Accumulation, and Clustering Timeline that enabled the detection of the critical locations where geohazard failures may initiate (21–23). This paper recognizes the crucial role of site conditions in determining the quality of satellite data for the selection of the most effective MTInSAR, and also discusses a site characterization and classification guide of the area of interest. The guide is designed to effectively characterize regions based on site conditions in view of satellite monitoring process, classifies sites with respect to the effect of site conditions on the quality and availability of radar data, and is a valuable tool for selecting the appropriate SAR method in monitoring and detection tasks. This paper summarizes the investigations, methodologies, approaches that led to the development of the workflow of the proposed monitoring system and demonstrates the ability of the proposed monitoring framework to identify critical locations of geohazard failure potential through implementation case studies.

#### **Methods**

The development of the technique that monitors the railway ROW for identifying critical locations exhibiting high-risk for geohazard initiation is based on the study of sites with a history of geohazard events, and/or availability of soil moisture measurements. The sites were monitored for a period of at least 12 months before the known event date using both archived and current satellite SAR data and typical PSInSAR and SBAS processes

Table 1. List of Study Sites with History of Geohazard Occurrence and Soil Moisture Data Records

ID	Site location	Coordinates (lat/long)	Event	Event date	Site class <sup>a</sup>
1	Lincoln, NE	40.70, -96.53	Derailment	6/25/2021	В
2	Birmingham, AL	33.47, <b>-86.95</b>	Stability monitor	Continuous	В
3	Maupin, OR	45.17, -121.10	Rockfall	5/7/2020	Α
4	Atlanta, GA	33.83, <b>-84.30</b>	Sinkhole	12/2021	С
5	Burlington, ND	48.25, -101.46	Derailment	5/1/2022	Α
6	Shiner, TX	29.43, -97.18	Derailment	6/3/2022	Α
7	Yellowstone, MT	43.64, -111.36	Landslides	6/16/2022	Α
8	Santa Clemente, CA	33.25, -117.37	Soil erosion	10/1/2022	Α
9	Sandstone WV	37.76, <del>-</del> 80.89	Rockfall/Derailment	4/9/2023	С
10	Raymond, MN	45.01, -95.23	Derailment	4/30/2023	В
11	Blackville, SC	33.36, -81.33	Soil moisture change	Continuous	В
12	Yosemite, CA	37.76, -119.82	Soil moisture change	Continuous	Α
13	Bodega, CA	38.32, 123.07	Soil moisture change	Continuous	A
14	Santa Barbara, CA	34.41, -119.88	Soil moisture change	Continuous	Α
15	Cortez, CO	37.26, -108.50	Soil moisture change	Continuous	A
16	Chatham, MI	46.33, -86.92	Soil moisture change	Continuous	В
17	Sandstone, MN	46.11, -92.99	Soil moisture change	Continuous	В
18	Stonehaven, Scotland	56.95, -2.32	Mudslides/Derailment	8/12/2020	Ċ
19	Pikeville, KY	37.34, -82.39	Landslide/Derailment	2/13/2020	Ď

<sup>&</sup>lt;sup>a</sup>Site class shown in the last column is based on the proposed classification guide.

reported in the literature. These sites are considered case studies that provide data and guide research activities. The collected site datasets were not used in a statistical framework. The findings of the study of these sites led to the development, implementation, and preliminary validation of the MTInSAR processing techniques with the Rolling Stack (RS) concept and the three postprocessing operations, that is, Thresholding, Scatterer Accumulation, and Clustering Timeline, and to the development of a site classification guide in view of the data quality and availability and site characteristics to facilitate the selection of the appropriate analysis tool.

#### Site Selection

Several sites are identified during the course of the work in coordination with Class I railroads and the Federal Railroad Administration. The preliminary selection of sites is conducted based on the event type and the need for site data collection for method development and approach validation. The events considered in this study are:

- Landslides
- Rockfalls
- Track settlement
- Embankment failure
- Slope failure
- Derailment
- Slope stability risk

• No event (for site data collection, routine satellite monitoring, or both).

Once the sites are identified, the availability of satellite data is investigated in regard to:

- Number of satellites monitoring the site
- Number of orbits of each satellite
- Availability and length of historic data for at least 12 months before the event.

Subsequently, the diverse site conditions that may affect the quality of the acquired satellite data are considered when evaluating the site. Such conditions include:

- Vegetation including seasonal variation and vegetation coverage level classified as (i) no vegetation, (ii) low/sparse growth (e.g., grass typically < 5 in.), (iii) medium growth, and (iv) tall/dense growth (e.g., tree canopy)</li>
- Soil condition (per OSHA classification) (24)
- Main soil type (silt/clay/sand)
- Topography and terrain
- Climate (e.g., rainfall, snow fall and snow cover, extreme weather conditions within a year)
- Seismicity
- Human-induced vibrations (e.g., blasts).

The selected sites are listed in Table 1 where the last column shows the site class as identified by the proposed site

classification guide discussed after the introduction of the analysis methods.

## Multitemporal InSAR Techniques

The image pairs referred to as interferograms were used in early studies to identify changes between the acquisitions and to obtain displacement in satellite lines of sight (LOS). Subsequently, the method was modified to incorporate a multitemporal approach (MTInSAR) in an effort to reduce errors in the displacement measurements and to enable tracking of surface changes over time. In contrast to the early InSAR analysis process that considers a single pair of SAR images, MTInSAR techniques combine interferograms derived from an extensive series of SAR images (stack of images) acquired within the period of observation. One of MTInSAR's key features is its ability to identify small surface changes over a long time. However, during the analysis period, if there is a sudden large change (>30 mm deformation, etc.) between any two acquisitions in the interferogram or the scatterer loses coherence as a result of other factors, MTInSAR analysis fails to monitor the change even if the surface is experiencing the deformation. The main difference among the multitemporal methods lies in how SAR image pairs are created. The PSInSAR and SBAS approaches are two MTInSAR techniques used for displacement measurements. The CCD timeline method is an alternate multitemporal technique that observes changes to surface properties and is used as an indicator for soil moisture change. The PSInSAR, SBAS, and CCD techniques are summarized in the following subsections while details on how the methods are adopted in this work are presented in Byrraju (25).

Interferometric Persistent Scatterer Synthetic Aperture Radar. The PSInSAR technique is one of the first developed MTInSARs (26) that employs fundamental InSAR principles over an extensive sequence of images to achieve highly accurate displacement measurements. The process begins with identifying PS in the observation area and can encompass a range of objects, including urban infrastructure like buildings, windows, roofs, and railway lines, as well as natural features like rocks and roads. The PS are identified by first creating InSAR pairs with one common master SAR image in the image stack, which is equidistant temporally from the first and last SAR image. PS are identified as individual pixels, or group of pixels, exhibiting consistent high coherence in all the image pairs throughout the analysis period (27) and are considered for displacement over time measurement. The image pairs are depicted graphically through connection graphs, which use the satellite acquisition date on the x-axis and the relative satellite position on the y-axis. An implementation example of the PSInSAR on the Maupin, OR site (ID 3) is shown in Figure 1. The connection graph is shown in Figure 1a and the computed deformation map is shown in Figure 1b. Blue deformation points indicate subsidence and red deformation points indicate the raising of the surface in the direction of the satellite's line of sight (LOS).

PSInSAR is effective in regions with many highly reflective surfaces with respect to satellite LOS. Highly reflective surfaces allow accurate measurement of surface deformations by transmitting most of the radar signal back. Regions like rocky, hilly terrain in the path of satellite LOS generate many stable PS that can be used to generate displacement data.

Small Baseline Subset. The SBAS technique is a variant of multitemporal differential InSAR analysis, which shares some similarities with PSInSAR. In contrast to PSInSAR, which primarily concentrates on observing deformation in coherent targets, SBAS analysis is primarily concerned with monitoring the progression of deformation in diffused radar targets or distributed scatterers (DS). The processing methodology of the SBAS technique exhibits numerous notable distinctions compared with PSInSAR. One prominent distinction is using multiple master files in the SBAS approach and is employed to mitigate the deterioration of coherence in InSAR pairs of PSInSAR as the temporal baseline expands in extreme pairs. The utilization of numerous master files results in a decrease in both temporal and geographical baselines, therefore enabling the assessment of deformation in DS. An implementation example of the SBAS on the Maupin, OR site (ID 3) is also shown in Figure 1, c and d. The connection graph is shown in Figure 1c and the computed deformation map is shown in Figure 1d. This difference in processing makes SBAS analysis particularly effective in areas with low concentrations of coherent targets because of temporal factors like seasonal vegetation growth. The ability to measure deformations when low PS is present makes it suitable for measuring deformations in rural regions. Unlike PSInSAR, where the deformation measurements are close to actual measurements, SBAS readings have a lower level of precision because of the low coherence threshold used in the development of deformation maps. In view of the deformation maps shown in Figure 1, b and d, it is noted that PSInSAR produces a lower density of deformation points than the SBAS at the same site using the same dataset. Furthermore, the SBAS deformation map shows a larger activity region, while the PSInSAR analysis shows the exact region where the rockfall event occurred.

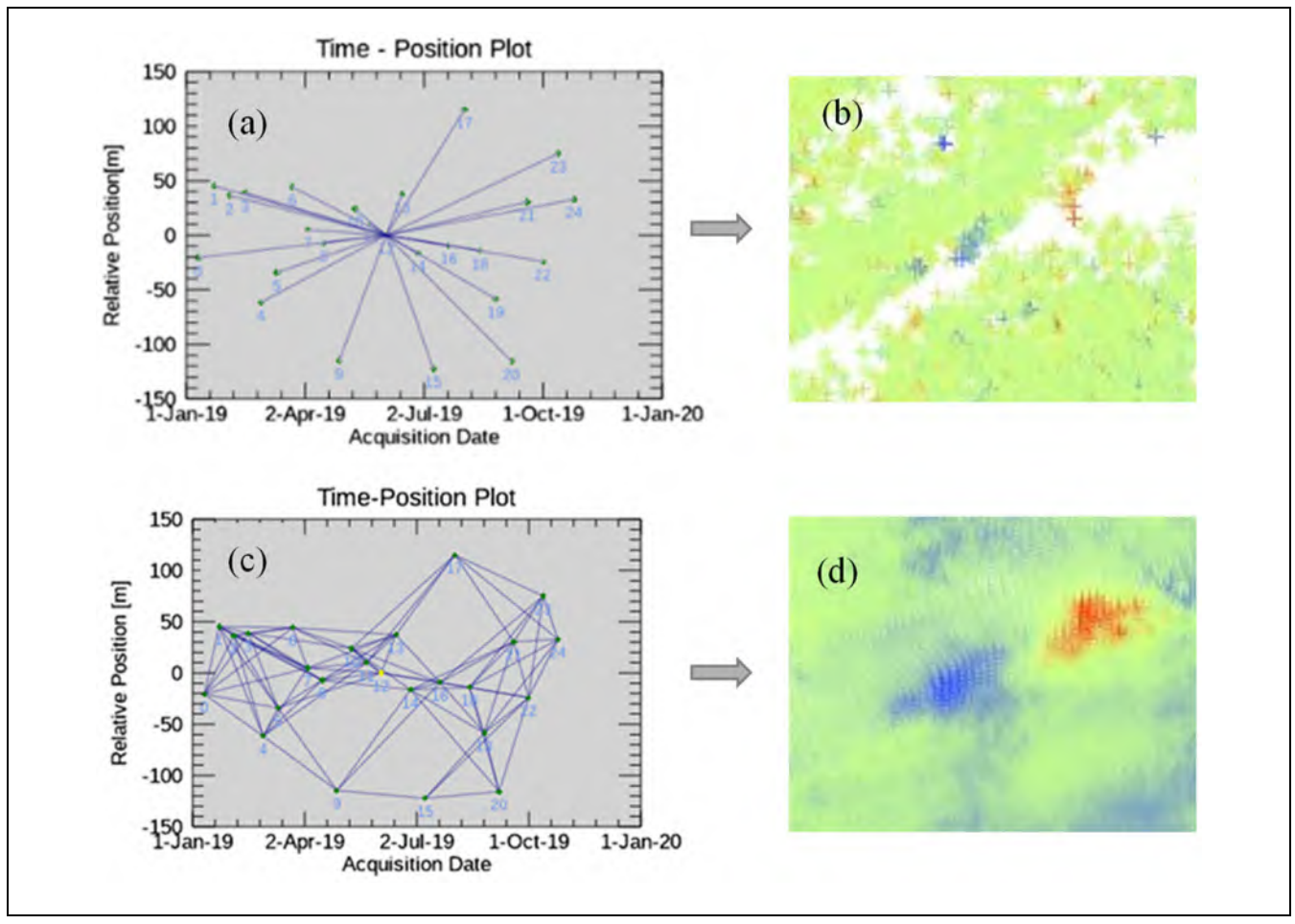


**Figure 1.** PSInSAR and SBAS analysis of Maupin Site ID 3: (a) PSInSAR image connection graph, (b) PSInSAR computed deformation map, (c) SBAS image connection graph, and (d) SBAS computed deformation map.

Note: PSInSAR = persistent scatterer interferometric synthetic aperture radar; SBAS = small baseline subset.

Coherence Change Detection Timeline. The CCD approach utilizes radar waves obtained from SAR imagery to identify changes that have taken place between two consecutive images. The sensitivity of the SAR sensor to changes allows the technique to detect subtle changes not visible in other methods. The coherence between the two images is evaluated by the sum of the spatial and temporal decorrelation of the signals, ranging from 0 to 1 (28). An area with 0 coherence has changed drastically between the image acquisitions, attributed mainly to moisture change, surface roughness, or a long time elapsed between acquisitions. While a single CCD analysis can identify critical surface and subsurface features, processing individual pairs of images is inadequate for monitoring a region over an extended period (29). Using a large stack of SAR images, the timeline method creates image pairs for CCD analysis based on the chronological order of the SAR images. An example of a CCD analysis is shown in Figure 2. Figure 2a shows the visual image of a site with a railroad track segment between points A and B clearly visible. Figure 2b shows a typical coherence image of the site showing high coherence along the track that is attributed to low moisture content in the track. Figure 2c shows decreasing coherence because of increasing soil moisture associated with rainfall event. Figure 2d shows the coherence along the track being completely lost attributed to very high soil moisture content resulting from prolonged intensive rainfall. The relationship between soil moisture content and coherence computed by the CCD was explored further to develop models of soil moisture change as a function of signal coherence that can be used in future studies to define threshold values of the triggering events and quantify the risk. This model was first introduced in Byrraju (22) and details of the development are reported in Li et al. (23). The model was developed with in-situ data from National Ocean and Atmospheric Administration (NOAA) sensors located at Site ID: 14, Santa Barbara, CA.

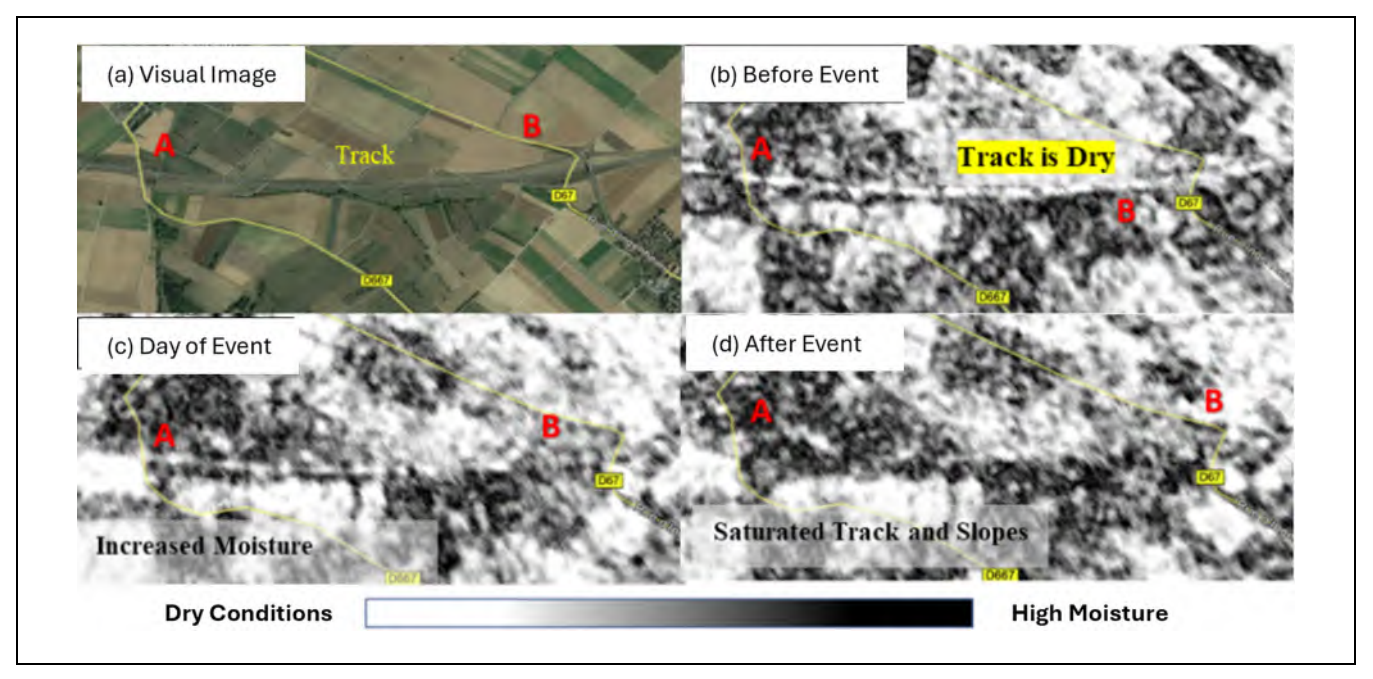


**Figure 2.** Example of coherence change detection (CCD) image analysis and correlation with water content: (a) visual image of site with a railroad track between point A and B, (b) a typical coherence image of the site showing high coherence along the track, (c) coherence along the track is changing because of increasing soil moisture, and (d) coherence along the track is lost because of high soil moisture content.

Rolling Stack-MTInSAR. MTInSAR's key feature is its ability to accurately identify small surface changes over a long time at each PS. However, if the coherence is lost at the scatterer during the analysis period as a result of a large change (e.g., movement > 30 mm) between two acquisitions or other factors, the scatterer is ignored, and the change cannot be monitored even if the surface is experiencing the deformation. Therefore, detection of critical areas through deformation monitoring using conventional MTInSAR is not possible. In such cases the proposed RS concept is implemented with MTInSAR techniques to detect and retain scatterers over longer time periods with very promising results. The proposed rolling stack-MTInSAR (RS-MTInSAR) limits the size of the stack of SAR images in the conventional implementation to several images that are necessary to preserve accuracy and to control noise, typically between 15 and 25, depending on the site characteristics and the particular MTInSAR method. Subsequently, site monitoring for a period of time that exceeds the time spanned by the stack is achieved by performing a series of MTInSAR analysis. Each analysis uses an updated SAR image stack where the first SAR image is dropped from the head of the stack and a new SAR image is added to the tail of the stack, creating an RS effect. Figure 3 demonstrates the concept assuming a monitoring period of one year, and temporal image acquisition baseline of 12 days yielding a total number of 30 SAR images.

Assuming for demonstration purposes only a stack size of 20 SAR images, 12 MTInSAR analyses need to be performed. Each analysis produces the geolocation of the PS, or DS, within the analysis stack as well as the time history of movement at each point. This information is considered in the postprocessing steps of the proposed method.

#### Postbrocessing Techniques

In the research, three postprocessing techniques were developed to identify regions within the area of interest with geohazard initiation potential. Thresholding identifies PS or DS points that are considered "high-risk" if the deformation at the point at any given time exceeds a threshold value. Scatterer Accumulation identifies the spatial distribution of the high-risk areas in a qualitative manner, while the Clustering Timeline analysis quantifies the rate of change of the precursors to the event initiation within the high-risk areas identified by the Scatterer Accumulation approach.

Thresholding. MTInSAR methods implement filters to treat temporal and spatial decorrelation of the signals to improve the quality of the deformation results, but only to a certain extent. Loss of coherence because of atmospheric contributions results in higher noise in the deformation measurements derived from the MTInSAR and

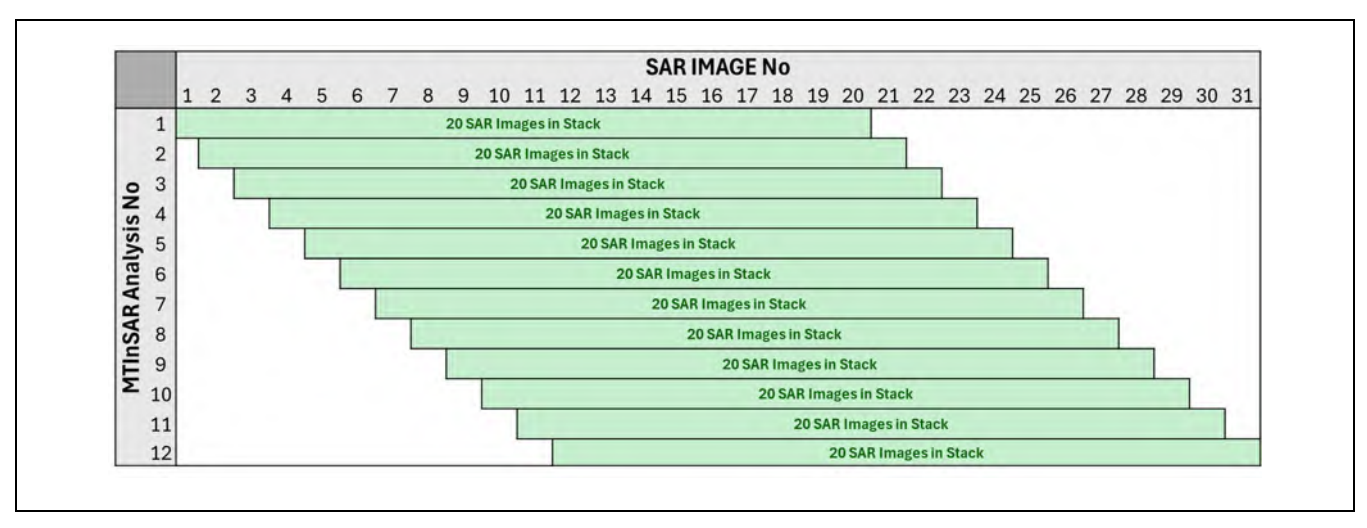


Figure 3. RS-MTInSAR analysis concept.

Note: SAR = synthetic aperture radar; MTInSAR = multitemporal interferometric synthetic aperture radar; RS-MTInSAR = rolling stack interferometric synthetic aperture radar.

Table 2. Recommended Threshold Values

Coherence	Theoretical precision (mm)	Threshold value $\pm$ (mm)
0.9	8	6
0.8	14	8
0.7	20	10
0.65	23	11
0.6	26	12
0.55	30	14
0.5	35	16
0.45	41	18
< 0.4	>50	20

hinders the detection of critical areas. The proposed Thresholding is a postprocessing filtering method implemented to all deformation analyses from the proposed RS-MTInSAR. The objective of the proposed filtering is to identify and remove the scatterers from the solutions that are formed by residual coherence losses from decorrelations, or represent points that, although they are properly identified, the exhibit small movement and are of no interest in the identification of the critical areas.

The criterion for the threshold is based on the coherence threshold used in the PS and DS identification process. In the case of PSInSAR, a coherence threshold of 0.7 is used as an indicator of PS, while in the case of SBAS, a coherence threshold of 0.3 is used as an indicator for DS points. The magnitude of the filter is determined by the theoretical precision of SAR deformation data as reported in Fiaschi et al. (30) and Bamler and Just (31).

The precision depends on the wavelength of the SAR sensor and the measured coherence. For example, for a C-band sensor and a scatterer with 0.7 coherence, the theoretical precision is 20 mm and any deformation above the theoretical is considered the true deformation. However, any deformation below the theoretical value may be masked by noise. In the proposed RS-MTInSAR, the theoretical precision should not be used as the threshold criterion because the coherence fluctuates in each SAR image pair in the stack. Thus, to prevent active deformation points from being filtered, conservative threshold values are recommended as presented in Table 2.

Scatterer Accumulation. The identification of the critical areas in the region of interest starts with establishing the Landsat optical image of the region to geolocate the scatterers. Landsat is publicly available through Google Earth. At the end of each RS-MTInSAR analysis the identified set of scatterers are filtered as discussed in the preceding "Thresholding" section and superimposed on the optical image of the region. For both event investigation and active monitoring, it is recommended that the monitoring period starts at least one year before the date of the event, or before the active monitoring commences. The scatterer accumulation will result in a continuously updated deformation map with the location of all scatterers appearing on the optical image. At this step, the critical locations can be identified by visual inspection, as areas where the density of accumulated scatterers increases over time. The detection of the critical locations, however, is implemented in a structured manner in the last postprocessing tool, that is, Clustering Timeline, discussed next.

Clustering Timeline. The last step in the proposed process for identifying the critical location within a larger monitoring region pertains to identifying the formation and progression of cluster of scatterers every time a new set of RS-MTInSAR analysis data becomes available. To this end, a grid is overlayed on the optical image with a subset size dependent on a combination of the desired resolution of the critical areas and the average number of the detected scatterers in the region. Higher risk areas are identified as those subsets, or group of subsets, that exhibit higher density of the clustered scatterers compared with their surrounding subsets. At this stage, although regions with a high potential for geohazard failure are identified, the imminency of the failure is not evident. A timeline analysis showing the rate at which the clusters are formed between any two successive datasets is used as an indication that a geohazard event failure is imminent. The timeline method is based on the geohazard observation that before the triggering event there is a rapid increase in density of the cluster in the geohazard vicinity.

## **Effects of Site Parameters on SAR Imagery**

Within this study's scope, several site parameters that influence the reliability of the MTInSAR methodology are identified, and their effect on SAR data is discussed. The parameters are classified into two categories: geometric parameters and surface parameters. The following sections provide further discussion on the topic.

### Geometric Parameters

Geometric parameters are influenced by topographic features like slope grade and the alignment of the said slope. SAR sensors are side-looking sensors that monitor a region with an angle of incidence. This influences the quality of data as some regions will not be illuminated by the sensor, and others will be partially illuminated. The illumination of these regions is dependent on the topographic features, which are geological parameters, and they affect the SAR sensor measurements through geometric interactions (32).

Slope Grade. The region under monitoring can be flat or have a sloped terrain. Regions that are flat reflect back-scatter based on surface properties like roughness, dielectric constant, and vegetation. However, regions with slopes are influenced by additional topographic characteristics like the steepness of the slope and its alignment. Monitoring steep slopes using SAR can be challenging

because of the geometric alignment of the topographic features. In cases of steep slopes, a phenomenon called layover occurs where the imaging shows the top part of the slope being laid over the lower section of the slope. The other effect of a steep slope is shadowing, where the SAR signal does not illuminate part of the region because of the intervening slope (28). Furthermore, these complex topographic conditions make it challenging to eliminate errors in deformation measurements. By taking into account the "local incidence angle," or the angle between the SAR look direction and the slope, a more sensible monitoring limit can be established. This range can be used as a rough guideline for the local incidence angle. As most SAR satellites have incidence angles between 20° and 50°, this establishes the slope limit at approximately  $50^{\circ}$  (33).

Slope Alignment. Slope alignment is a topographic feature that affects the backscatter of SAR satellites. Current SAR satellites are polar orbiting, that is, they orbit around the poles for each revolution and monitor Earth's surface (34). Since the direction of the satellite is constant, when the SAR LOS direction is in the same direction as the slope, the SAR's sensitivity to movement along the slope is maximum. In conditions where the slopes will be directly facing the satellite, the sensitivity to slope movement is reduced since the displacement should cross a threshold in the satellite LOS before it can be detected (35). This phenomenon can be seen in the case of SBAS deformation analysis of a rockfall event shown in Figure 4 at a location marked by the red square. As a result of regional properties like rocky terrain, this region has high backscatter. Although the surface properties of the region were supposed to generate large backscatter, the look angle contributed the most in monitoring the region. Data captured from two different orbits of the same satellite, Sentinel-1, are considered. In the first orbit analysis shown in Figure 4a, the LOS of Sentinel-1B is in the same direction as the slope movement within the red square and, thus, the component of the movement in the direction of the LOS is significant and was noticed eight months before the event took place. On the other hand, the same region was observed using Sentinel-1A, where the slope is facing the satellite, the sensitivity to deformations was low, and the deformations were not observed until one month before the event took place, as seen in Figure 4b.

## **Surface Parameters**

Surface characteristics like surface roughness, soil moisture, vegetation, and soil type influence surface scattering. These parameters influence the amount of radar signal reflected back to the sensor and thereby affect the quality

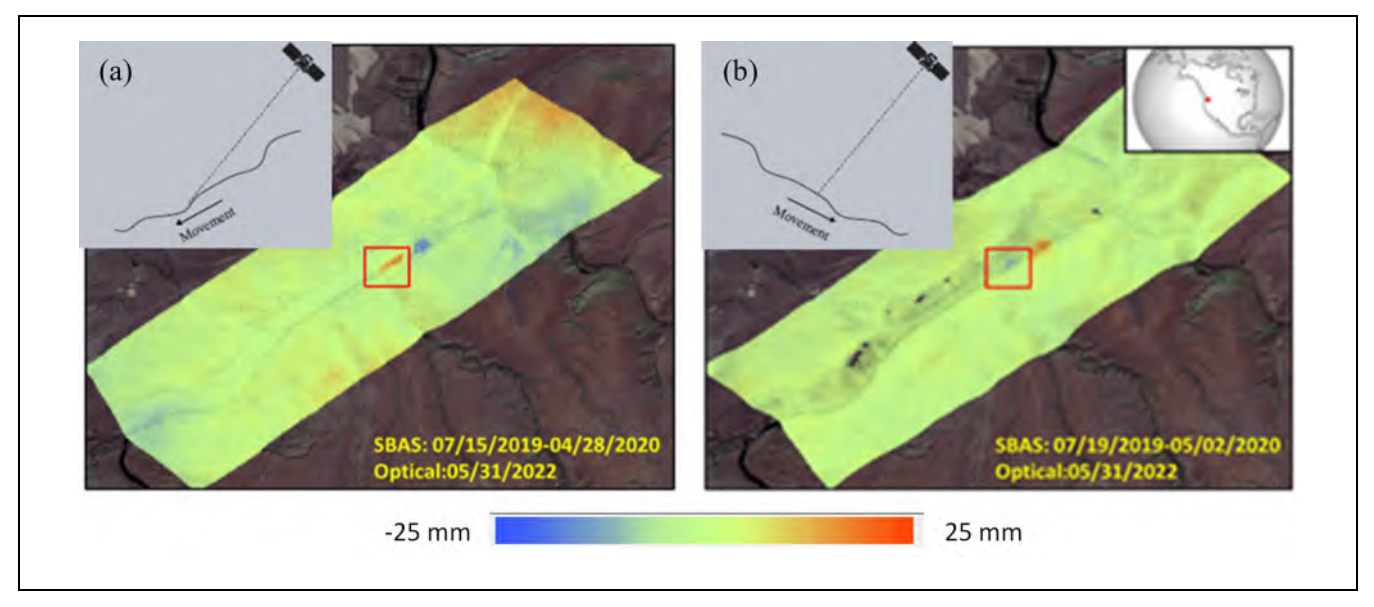


**Figure 4.** Effects of slope alignment on deformation measurements—Maupin, OR site: (a) Sentinel-IB LOS is in the direction of the slope and causes maximum sensitivity to SAR measurement of ground movement and (b) Sentinel-IA LOS is perpendicular to slope causes low SAR sensitivity to SAR measurement of ground movement.

Note: LOS = lines of sight; SAR = synthetic aperture radar; SBAS = small baseline subset.

of the monitoring process (36). This study uses a C-band radar onboard satellite Sentinel-1 that has a 5.5 cm wavelength, and its interactions with surface parameters are discussed in the following subsections.

Surface Roughness. The main factor controlling how radar signals bounce back from a surface is its roughness and the target's dielectric constant. A smooth and flat surface will reflect the incident radar wave away from the radar and is known as specular scattering. In these conditions there will be no scattering of energy back toward the radar unless the surface is facing the radar. Because the majority of natural surfaces are not perfectly smooth, the scattering of the incident radar wave is diffused in a variety of directions, including back again toward the radar (37). Surfaces with a higher degree of roughness disperse more energy in all directions, including the direction toward the radar. For the purpose of better illumination, a surface should be "rougher," which means the height variations of the surface should be large (34). Surface roughness can be quantified based on the root mean square height,  $h_{rms}$ , of the mean height of the surface into three categories, that is, smooth, intermediate and rough as

Smooth: 
$$h_{rms} < \frac{\lambda}{25\cos\theta}$$
  
Intermediate:  $\frac{\lambda}{25\cos\theta} < h_{rms} < \frac{\lambda}{4\cos\theta}$  (1)

Rough: 
$$h_{rms} > \frac{\lambda}{4 \cos \theta}$$

The surface roughness is directly related to satellite wavelength  $\lambda$  and inversely related to the cosine of the incident angle  $\theta$  (38). The area for surface roughness measurement is the resolution cell, which is the smallest distinguishable area that a radar system can differentiate (39). This study does not directly measure surface roughness for the purpose of site classification. Instead, it uses an existing database that categorizes surface roughness according to the soil type (40–42).

Dielectric Constant. A material's dielectric constant indicates how it affects the transmission of electromagnetic waves. The dielectric constant of the majority of natural materials falls somewhere in the range of 3 to 8 when the material is dry. However, the dielectric constant of liquid water is approximately 80. Therefore, the quantity of water present in the target, regardless of its form (such as soil moisture or vegetation water content), significantly affects the radar backscattering (43). A higher percentage of liquid water raises the dielectric constant and decreases the radar wave's ability to penetrate the target. The amount of liquid water in the target can change as a result of environmental conditions, and this change can be easily observed in SAR images and their multitemporal interferometric combinations (34). It should also be important to consider that the presence of soil moisture has minimal effect on the quantitative error in deformation studies; it mainly affects the signal strength (44), and thus the ability of the methods to detect and retain PS points. Although the dielectric constant greatly influences the backscatter of a region but not the accuracy, it is not considered a factor for site classification for deformation measurements since it changes rapidly and requires accurate site readings that are difficult to track. However, it is utilized as a factor in CCD, which depends on the change in backscatter as an indicator of soil moisture change (45).

Vegetation. There are intricate and varied relationships between the various types of vegetation and the scattering processes that result caused by big differences in their geometric shape and density of plants. Leaves, tree trunks, grass blades, and shrubs in a variety of forms can all be considered scattering elements. The dielectric changes that are brought about by variations in the amount of water present in the soil and canopy have a significant impact on the backscattered intensity that is measured in agricultural areas. Similarly, the forests also exhibit significant variations in forest backscatter because of fluctuations in soil and canopy water content. The scattering coefficient of such radar targets is defined by the scattering characteristics of the individual items, their spatial distribution within the layer, and the medium's dielectric constant (34). As a general rule, a C-band radar sensor cannot penetrate deep and is more sensitive to the structure of the canopy. The backscattering signal, in most cases, gets trapped within the canopy, and low backscattering occurs. The backscattering increases in dry and fall conditions when there is low leaf cover (46). C-band SAR sensors can be used for short (less than 12 cm in height) and, in some cases, medium vegetation (12-45 cm). Areas with large vegetation are difficult to monitor for deformations as a result of complex factors involved in the backscattering mechanism (47).

Surface Wetness. Flooding a region can cause a significant alteration in the backscatter signature of the affected area. The backscatter in regions with a low-forest canopy will increase suddenly because the radar signal will bounce with the forest and reflect back to the sensor ("double bounce"). In contrast, if the region has no forest and the plain surface is flooded, the region will lose its backscatter as the radar signal bounces away from the sensor ("specular reflection") (34). The sudden change in the scattering principle is because of water covering the surface roughness and making the surface completely smooth.

#### Site Characterization and Classification

It is evident in the preceding discussion that a site characterization and classification guide is desired to guide the selection of the appropriate tools for monitoring the railway ROW and detect locations at higher risk of geohazard initiation. The proposed guide accounts for the predominant factors affecting the quality of results as identified in this study in view of the availability of satellite SAR data for the site.

Four distinct categories, A, B, C, and D (good to bad) are established to classify sites based on their potential for facilitating successful studies. The availability and quality of the satellite radar signals, as it relates to noise affecting the analysis results, guided the definition of the "four site classes." Class A (ideal) is associated with minimum or negligible effects of noise in the results. Class B (normal) is associated with moderate noise that its source is identifiable, it is directly related to site conditions, and is typically steady over time. Class C (noisy) is associated with higher noise levels that may vary over time and is typically attributed to multiple sources. Class D (dark) sites are associated with sites that are either not visible by any satellites, or the noise is so high that the results are deemed unreliable.

## SAR Data Availability

Sites should have access to extensive stacks of satellite data (over 12 months) to effectively monitor the region. Regions with less than 7 months of data are automatically classified as "C" class. The low classification is given because of the inability to perform multitemporal SAR analysis. If the region has access to multiple satellites, the classification guide is applied for each satellite, and the highest classification is chosen as the site classification. In many cases, if an area is inaccessible or classified as a lower tier by one satellite, its classification improves when viewed from an alternate angle or through an additional satellite.

The site parameters directly influencing the proposed site classification in order of priority are: (i) slope grade, (ii) slope alignment, (iii) vegetation, (iv) surface roughness, and (v) surface wetness. The classification process is captured in a chart shown in Figure 5. The classification process starts by identifying the slope grade and potential slope alignment. These are prioritized because the sensor covers a large area  $(250 \times 250 \, \mathrm{km})$ , and topographic features are the most significant influences on the classification. Next, the process considers surface parameters that can affect classification on a more regional level.

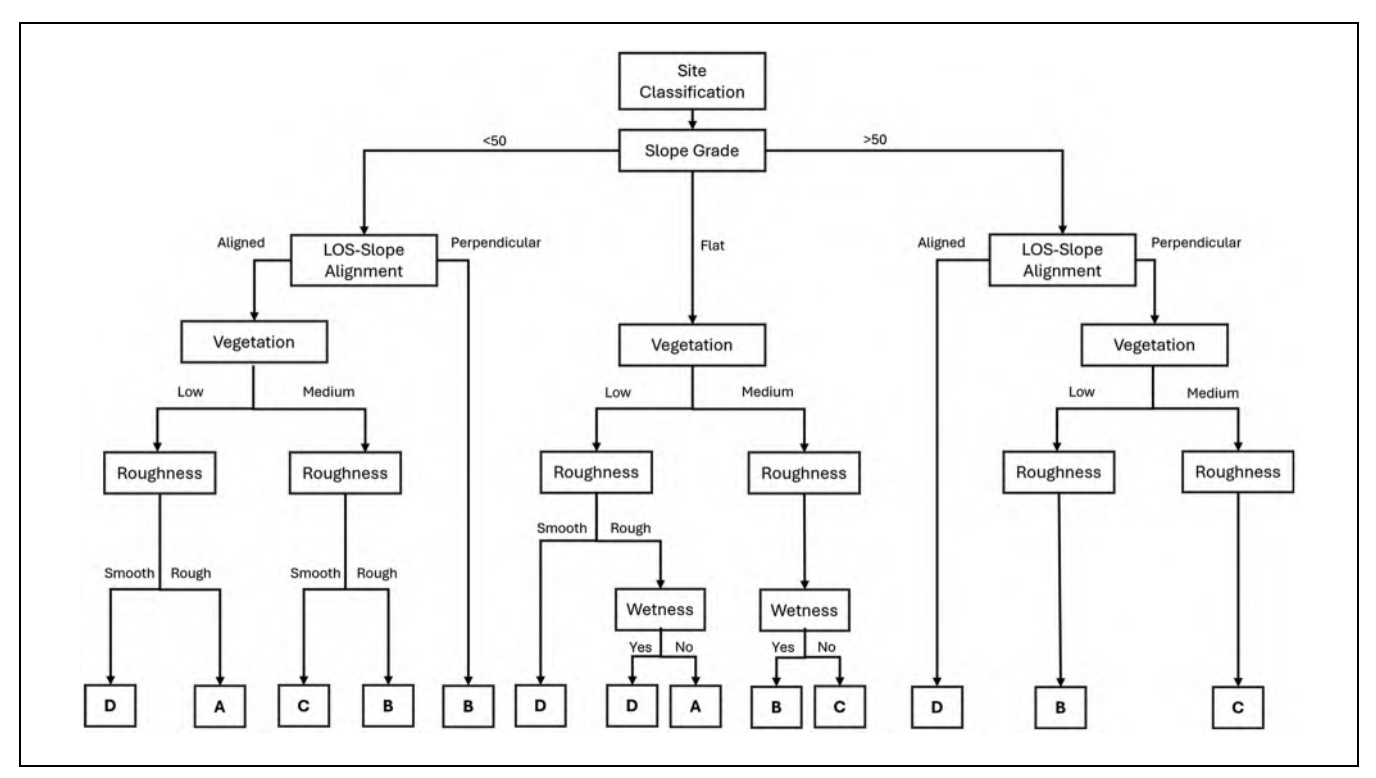


**Figure 5.** Site classification chart. *Note*: LOS = lines of sight.

Slope Grade. The slope grade is classified into three categories based on the incidence angle of the observing satellite. Regions with slope values greater than 50° have a higher chance of geometric distortions like layover, shadowing, and overlaying effects. Flat terrain has additional influences like surface wetness, which do not influence regions with slopes (33).

Slope Alignment. The slope alignment is classified into two categories: (i) slope aligned with the LOS, and (ii) slope directly faces the satellite, that is, perpendicular to LOS. Large-scale deformations are still detected in case (ii), and conventional InSAR can still be used for monitoring and early warning systems. Finally, regions with large slopes not facing the satellite cannot be monitored because of the shadowing effect.

Vegetation. After slope alignment, the radar signal first interacts with vegetation before it interacts with the surface. Two cases are considered: (i) low vegetation (<12 cm) and (ii) medium vegetation (12–45 cm). The proposed guide does not consider data from sites with large vegetation (>45 cm) as no backscatter is available from these conditions and the site should be classified as D.

Surface Roughness. Since this study does not measure the exact surface roughness of the region, the monitoring is divided into only two categories: smooth and rough. Regions with slope in the look direction of the SAR sensor require surface roughness for backscattering. When the region is smooth, the signal gets reflected away; this signal loss leads to a classification of D. The presence of vegetation helps in some smooth terrains where the radar signal gets reflected because of the vegetation acting like a rough surface. In conditions where the surface is facing toward the sensor, the surface roughness does not influence to the degree as it would other terrain conditions.

Surface Wetness. Surface wetness causes the surface roughness of the region to be converted to a smooth surface, causing the specular reflection to the radar signal, that is, the signal gets reflected away. The only conditions where the surface wetness can improve the results would be when additional elements like vegetation or manufactured structures cause the reflected radar signal to go back to the sensor (47).

Representative examples of each site class are shown in Figure 6 followed by a descriptive characterization.

Class A (ideal): This site class is associated with strong signals where the noise as a result of site



**Figure 6.** Examples of site classes: (a) Class A—Site 5, Burlington, ND, (b) Class B—Site 2, Birmingham, AL, (c) Class C—Site 18, Stonehaven, Scotland, and (d) Class D—Site 19, Pikeville, KY.

characteristics has minimum or negligible effects on the analysis results. Examples include flat terrain and hilly/mountainous terrain (when slopes follow the satellite line of sight), minimal vegetation coverage without significant seasonal variation, multiple satellites and/or orbits, and at least 24-month satellite historical data are available with multiple orbit directions. Figure 6a shows an example of a Class A site.

Class B (normal): This site class is associated with signals where the noise as a result of site characteristics has moderate effects, its source is identifiable, it is directly related to site conditions, and is typically steady over time. Examples include open terrain, rolling hills, short escarpments, minimal vegetation coverage without significant seasonal variation, and at least 12-month satellite historical data available. Figure 6b shows an example of a Class B site.

Class C (noisy): This site class is associated with higher noise levels that may vary over time and are typically attributed to multiple sources. Examples include hilly/mountainous terrain (when slopes face away from satellite line of sight) with medium to dense and tall vegetation with significant seasonal variation, escarpments, less than 12-month satellite

**Table 3.** Preferred Method Selection for Critical Location Identification Based on Site Class

		Site clas	ss	
Method	Α	В	С	D
PSInSAR	/w Th	/w RS & CT	NA	NA
SBAS	NA	/w RS, SA & CT	/w RS & SA	NA
CCD	/w Th	/w Th	/w Th <sup>a</sup>	NA

Note: PSInSAR = persistent scatterer interferometric synthetic aperture radar; SBAS = small baseline subset; CCD = coherence change detection; RS = rolling stack; Th = thresholding; SA = scatterer accumulations; CT = clustering timeline; NA = not applicable.

historical data available, or intermittent data availability. Figure 6c shows an example of a Class C site.

Class D (dark): These are sites that are either not visible to the satellite, and there is no line of sight, or the noise is so high that the results are deemed unreliable. Examples include mountainous terrains, gorges with dense and tall vegetation, tall escarpments, and dense vegetation coverage without significant seasonal variation. In some conditions,

<sup>&</sup>lt;sup>a</sup>Coherence change measured from the surrounding region.

these sites may be ideal in terrain profile but be located in satellite blind spots. Figure 6d shows an example of a Class D site.

After a site has been classified, the most appropriate method can be selected from Table 3.

# Cross-Evaluation of Satellite Analysis with Other Data Sources

Once a satellite data analysis set is complete for a specific site, the findings are cross-evaluated with one, or more data types from other sources that will facilitate detection of critical areas. Such data sources include optical imagery, topographic profiles, meteorological data, soil profiles, and soil moisture.

## **Optical Imagery**

To accurately identify deformation by InSAR and to track changes in land cover, optical imagery is crucial. Optical imagery shows changes in the environment caused by human activity or other sources and can be used to determine if deformation is environmental or caused by human factors. Linking surface changes seen in the imaging with ground motions enhances InSAR data. Optical photography, for example, might show urbanization or deforestation, causing landslides or subsidence. This combined approach improves our understanding of these occurrences by connecting deformation episodes to surface alterations and patterns of land use. Optical imagery is utilized from two sources. Landsat satellite data provides higher resolution but a high revisit time of 1 year. The other source is the Sentinel-2 satellite, which has a revisit time of 12 days but low resolution. Landsat is publicly available through Google Earth and Sentinel-2 is obtained from the Sentinel satellite data hub with the European Space Agency (48) and the Alaska Satellite Facility (ASF) (49).

## Topographic Profiles

Topography affects phase shifts, coherence, and radar signal propagation, considerably affecting InSAR. Geometric distortions such as foreshortening, layover, and shadowing can occur in areas with steep or rugged terrain, making it more difficult to discern surface displacement. Topography can also increase errors and decrease coherence, particularly in places with steep slopes. Topographic data are utilized in two stages. The optical image for the area of interest is observed to obtain initial topographic properties, followed by an indepth analysis from United States Department of Agriculture (USDOA) surveys.

## Meteorological Data

Meteorological data like rain and snowfall play a crucial role in understanding the impact of environmental conditions on SAR radio waves. Rainfall, in particular, can significantly affect InSAR coherence by altering surface properties and causing a correlation between radar acquisitions. When rain increases soil moisture or promotes vegetation growth, the ground's dielectric properties change, leading to a loss of coherence, especially in vegetated or agricultural areas. Rainfall data are obtained from three different sources based on the requirement. The first two are from the NOAA's USCRN program and sensors deployed in the field. The third is from commercial websites like the Weather Company (50), which reports hourly weather forecasts based on data from the National Weather Service and different personal weather stations.

#### Soil Profiles

Soil profiles, with their diverse layers and unique physical properties, are a key element in SAR data interpretation. The composition and structure of these layers, encompassing factors such as soil texture, moisture content, and surface roughness, dictate the nature of radar signal interaction with the ground, thereby influencing InSAR analyses. The impact of soil texture on the penetration depth of the SAR radar wave, and consequently on the signal strength and SAR coherence, shows the importance of soil profiles. A region's soil profile is obtained from annual soil surveys conducted by USDOA. These data are county-based and available from USDOA service centers like "websoilsurveys" (51). These surveys contain essential information such as the type of soil, soil profile, the height of the water table, the water drainage class, and the slope properties.

#### Soil Moisture

Soil moisture significantly affects the behavior of SAR signals, influencing both the backscatter intensity and coherence of the radar data. The dielectric properties of soil change as moisture content increases, directly affecting how radar waves interact with the ground. Therefore, the satellite analysis data needs to be cross-examined with soil moisture conditions. Soil moisture data are obtained from open-sourced ground-based sensors from the USCRN program (52), which collect ground soil moisture and weather over distinct observation points nationwide. These sensors provide data daily for a roughly 1 km area. Alternatively, soil moisture sensors are deployed by researchers to monitor a given region to obtain soil moisture every 5 min, with the location of sensors being known to be 1m in precision.

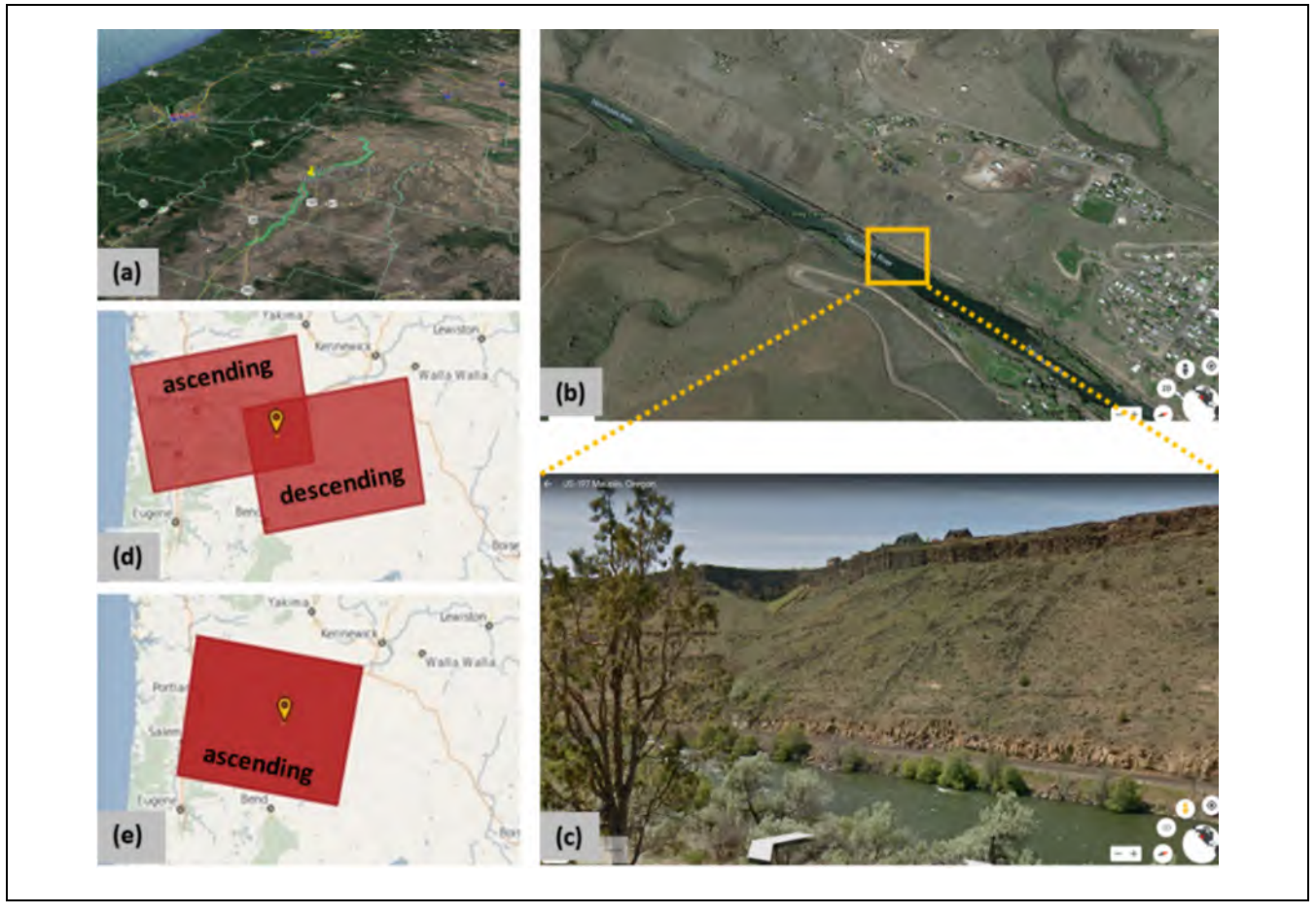


**Figure 7.** Site ID 3: Maupin, OR (a) Google Earth image of site, (b) Google Earth closeup view, (c) street view of site, (d) Sentinel-IB paths, and (e) Sentinel-IA path.

# Implementation Example: Site ID 3—Maupin OR

This section presents a case study that demonstrates the implementation of the classification guide and the employed methods. The case study pertains to site ID 3—Maupin, OR, listed in Table 1 and is among the first case studies considered in this work (22). Further details are reported in Byrraju et al. (22) while analysis results of all studies can be found in Byrraju (25).

## Case Study Site

In the early morning of May 7, 2020, a derailment occurred because of a rockfall near Maupin in Oregon, as shown in Figure 7, a and b. The derailment took place approximately 0.71 mi from the city center. This region has slopes between 40° and 70° and is well drained, as shown in Figure 7c. The area of interest encompasses 5.85 mi<sup>2</sup> and is characterized by the top 4 in. of the soil being extremely stony loam, with the bedrock lying

12–20 in. deep (53) This region has access to multiple satellites with both satellites facing the monitoring region. In view of the site classification chart in Figure 5 the site is classified as A.

## Data Availability

The study area is on the West Coast and benefits from multiple satellite passes, providing access to SAR data from different angles. The site has high radar reflectivity with minimal signal losses. The dataset for this study is obtained from the Sentinel constellation, and the satellite images are downloaded from the Sentinel-1 EU datahub (48) and ASF (49). Figure 7d shows the area captured as the Sentinel-1B satellite approaches (ascending path) the site and as it is leaves (descending path) the site, and Figure 7e shows the area captured on the path of Sentinel-1A satellite. The analysis employs PSInSAR, SBAS, and CCD techniques using archived satellite radar images spanning 24 months, covering the event's occurrence. To ensure accurate results, the study is

<b>Table 4.</b> Satellite Data Acquisition Periods for Maupin O	Table 4.	Satellite Data	Acauisition	Periods :	for	Maupin	OR
---	----------	----------------	-------------	-----------	-----	--------	----

Dataset	Sentinel-IB ascending	Sentinel-1B descending	Sentinel-IA
Pre-event	6/1/2019 to 5/2/2020	6/21/2019 to 4/28/2020	6/16/2019 to 5/5/2020
Postevent	5/14/2020 to 1/9/2021	5/10/2019 to 4/6/2021	5/17/2020 to 12/31/2020

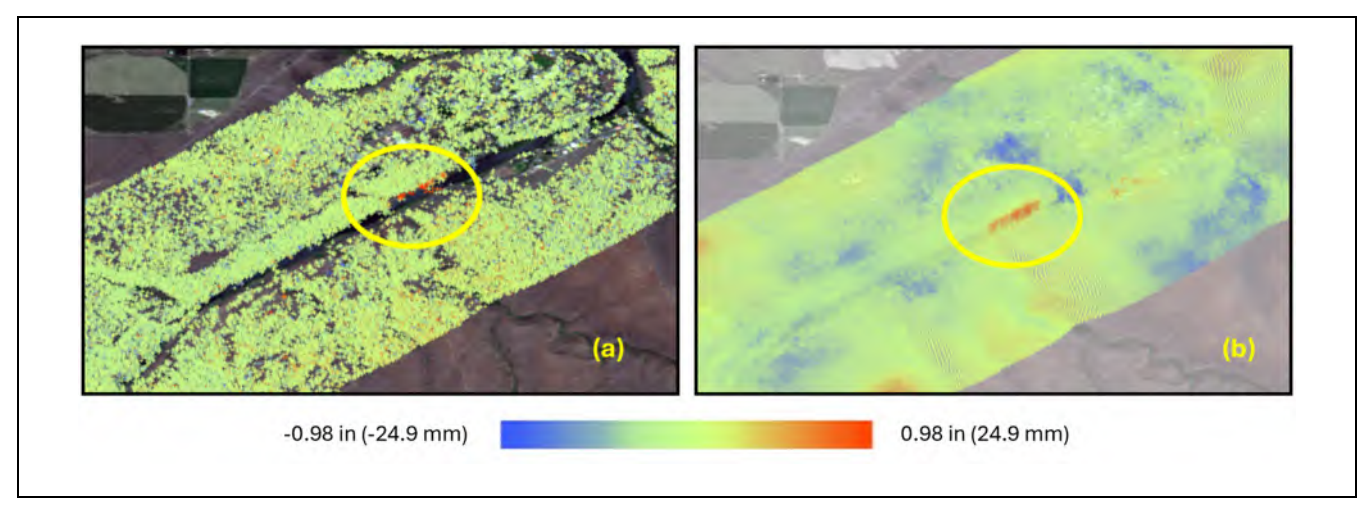


**Figure 8.** Deformation map of site ID = 3 as obtained from: (a) PSInSAR analysis and (b) SBAS analysis. *Note*: PSInSAR = persistent scatterer interferometric synthetic aperture radar; SBAS = small baseline subset.

divided into two periods—pre-event and postevent. Separation is essential since events such as rockfalls can cause sudden subsidence and significant changes in the Digital Elevation Map (DEM), leading to a loss of coherence and PS, affecting data quality. The acquisition periods are detailed in Table 4.

## **Deformation Monitoring**

The PSInSAR and SBAS analysis for site mobilization monitoring was conducted using a stack of 20 and 25 images respectively, at a minimum. The deformation maps from the three orbits are superimposed on an optical image taken on April 10, 2020. The displacement observed is plotted on the color-coded PS images that show the total displacement over the entire analysis. The negative displacement (blue) indicates subsidence, and the positive displacement (red) denotes height gain with respect to the line of sight of the satellite acquisition.

Pre-Event Analysis. The PSInSAR and SBAS analyses over the period June 2019 to April 2020 produced the deformation map shown in Figure 8, a and b, respectively. Both analyses reveal that while the area of interest remains "quiet" during the monitoring period, the area within the area marked by the yellow circle mobilizes

months before the event occurrence. The PSInSAR analysis identifies individual PS points that can be monitored throughout the monitoring period. The SBAS analysis identifies such points in an average sense.

Figure 9 displays the change in position of one PS point with the most substantial displacement over the analysis period. The highlighted area where the rockfall occurred was relatively quiet until the end of September 2019, period T1 in Figure 9. The region experienced high displacement in the period T2 until the start of December, followed by a brief stable period, T3, before it experienced high displacement leading to the rockfall, T4. This indicates that for at least eight months before the event, the region experienced a change in position, compared with the broader area. At the start of the observation period, the deformation changes were because of noise.

Postevent Analysis. A postevent PSInSAR analysis has been conducted on all three orbits after the event, and the results have been combined to generate the deformation map in Figure 10. The area within the red square shows no significant displacement, indicating that the region is not undergoing any surface movement and is now in a state of equilibrium.

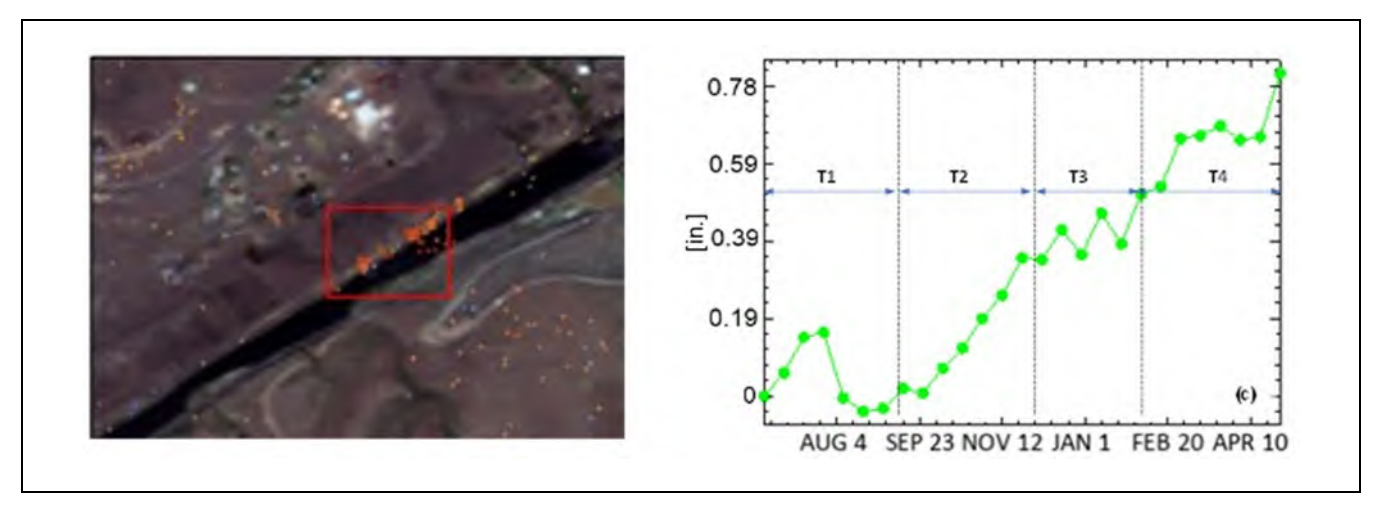


Figure 9. Displacement over time of one PS (Persistent Scaterer) point.

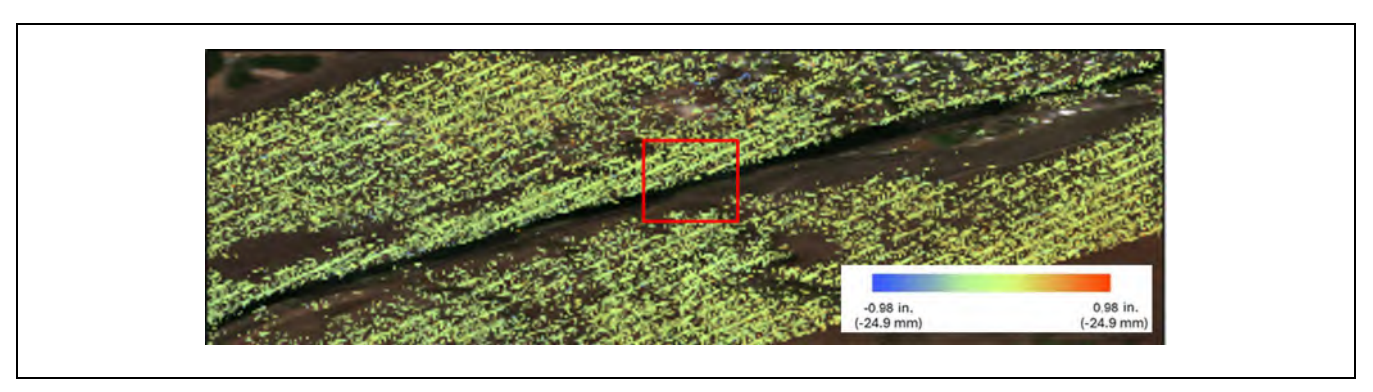
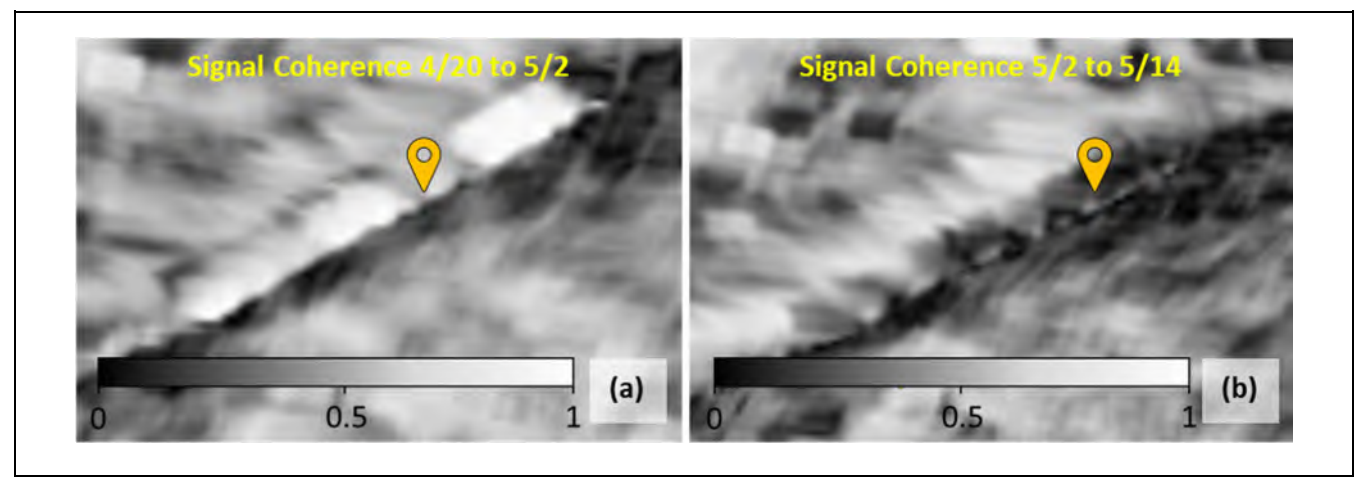


Figure 10. Postevent analysis total deformation map of persistent scatterers. No significant position change noted.



**Figure 11.** Coherence maps: (a) 12-day period right before the event and (b) coherence during the event.

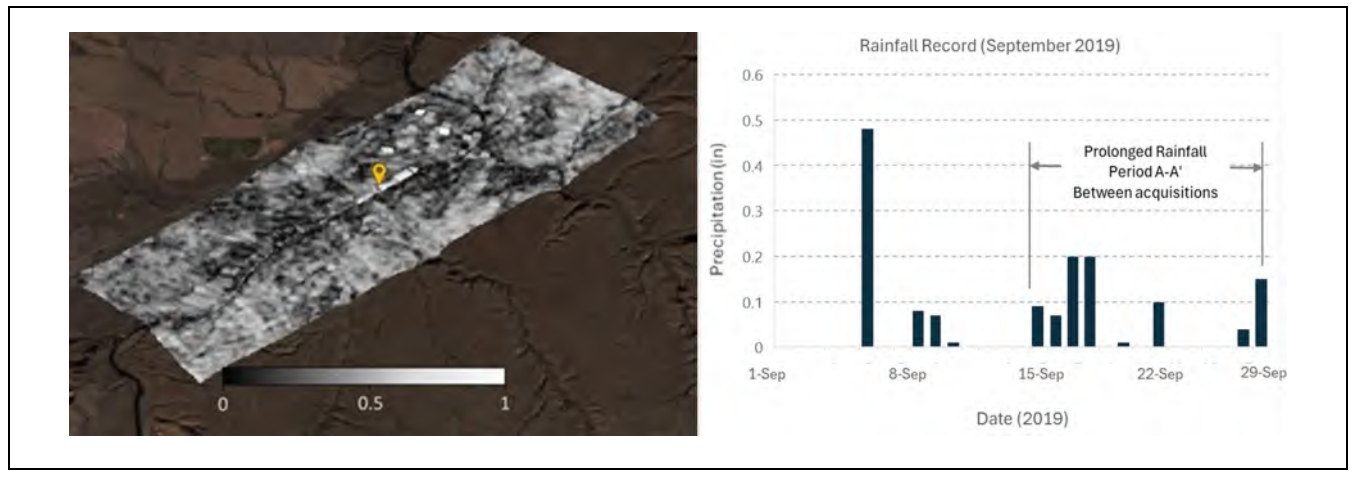


Figure 12. Rainfall records for the month of September 2019 and associated coherence map.

## Coherence Change Detection Monitoring

A CCD analysis is also conducted during the observation period. The complete analysis is reported in Byrraju (25). An example of the coherence change is shown in Figure 11. Figure 11a exhibits the coherence image from the analysis between an image pair captured on April 20 and May 02 (right before the event), demonstrating high coherence in the broader area of the event but noticeable coherence loss in the immediate region of the event. Figure 11b portrays the coherence analysis of the region studied using data from May 2 to May 14, that spans over the May 7 event date. The noticeable coherence loss in the immediate area of the event is attributed to the surface changes caused by the rockfall.

## Cross-Evaluation with Other Data Sources

The findings from the PSInSAR and CDC analysis are evaluated next in view of rainfall, topography and soil information in the area of interest. The coherence images generated by CCD analysis can provide further insights into the rockfall event. As evidenced in Figure 9, mobilization of the site started after September 2019. The coherence map for the period September 17 to September 29, shown in Figure 12, reveals a low coherence in the region of the rockfall event marked by the yellow marker. Since the site is still "quiet" and no geometry changes are detected, the low coherence over the broader region could be attributed to the other major factor that affects it, that is, change in soil moisture in the surrounding area. This observation is verified by the rainfall records for the site depicted in Figure 12 for the entire month of September.

According to the soil information for the area (53) and Figure 7c, the immediate region of the rockfall is a

steep, rocky slope where surface runoff is at fast rates, without any ponding or retained water; this is consistent with the high coherence for most of the analysis period in the immediate region. The broader area, however, is relatively flat, and precipitation seeps through the soil changing the soil moisture content; this is consistent with the coherence loss after rain periods.

## Validation Study

The RS-MTInSAR with Thresholding, Scatterer Accumulation, and Clustering Timeline analysis were first validated through implementation to sites not included in the development of the proposed approach, using both SBAS and PSInSAR analyses and have been reported in Byrraju (25) and Byrraju and Rizos. This section presents a case study that considers Site ID 9 for the validation of the method that is based on the RS-SBAS analysis. Site ID 9 was assigned by the industry sponsor at the later stages of the research and serves as a case study for the validation of the proposed technique.

### Study Site and Incident Summary

A freight train near Sandstone, West Virginia, Figure 13a, derailed when it hit a rockslide, Figure 13b, causing injuries to three crew members and resulting in the release of diesel gasoline into the nearby river Figure 13c. The yellow dotted box in Figure 13a indicates the site of the rockfall incident that occurred in the early hours of Wednesday, March 8, 2023. The collision in the early morning locomotive footage reveals that the debris blocking the railway path caused the derailment. Furthermore, on careful examination of the images reported in the media, it becomes evident that there are



Figure 13. Validation study site: (a) incident site, (b) derailment, (c) locomotive view of rockfall, and (d) two distinct slope failures ~100 m apart.

Table 5. Site ID = 9: Analysis Datasets

Dataset	Sentinel-1A
Analysis I	10/14/2021 to 09/03/22
Analysis 2	11/19/2021 to 10/09/22
Analysis 3	12/13/2021 to 11/02/22
Analysis 4	01/30/2022 to 12/08/22
Analysis 5	03/07/2022 to 01/13/23
Analysis 6	05/06/2022 to 02/18/23
Analysis 7	06/23/2022 to 03/02/23

two well-defined surface area regions that experienced slope failure, with an approximate distance of 100 m between them, as evidenced in Figure 13d.

The derailment site is about 1 mi from Sandstone and is located between a cliff on one side and the New River on the other. This region has a 35% to 80% slope and is well drained. The area of interest has decaying plant matter and silty clay loam on the top 4 in. with stony silty clay loam underneath. The cliff facing the railway track has a stony profile, with the region above the cliff having dense forest cover. Based on the preceding factors, the

site is classified as C, according to the site classification guide.

#### Dataset and RS-SBAS

The region under investigation is covered by Sentinel-1A, also shown in Figure 13a by the area marked in red, with a frequency of acquisition of 12 days. The region is located in a rural area with radar signals blocked by the cliffs facing away from the satellite path. As a result of the geolocation of the incident area, a low number of PS points is expected. The Sentinel dataset for this study is downloaded from the Sentinel-1 EU datahub and ASF. The region also has a high cloud presence, reducing the number of optical images available from Sentinel-2. In view of the relatively low site class, it was decided to employ the RS-SBAS technique with an image stack size of 25. The data acquisition began on November 14, 2021, and continued until March 2, 2023, a week before the event. A total of 44 acquisitions were obtained for the analysis yielding seven SBAS analyses for the chosen 25-image RS, as presented in Table 5.

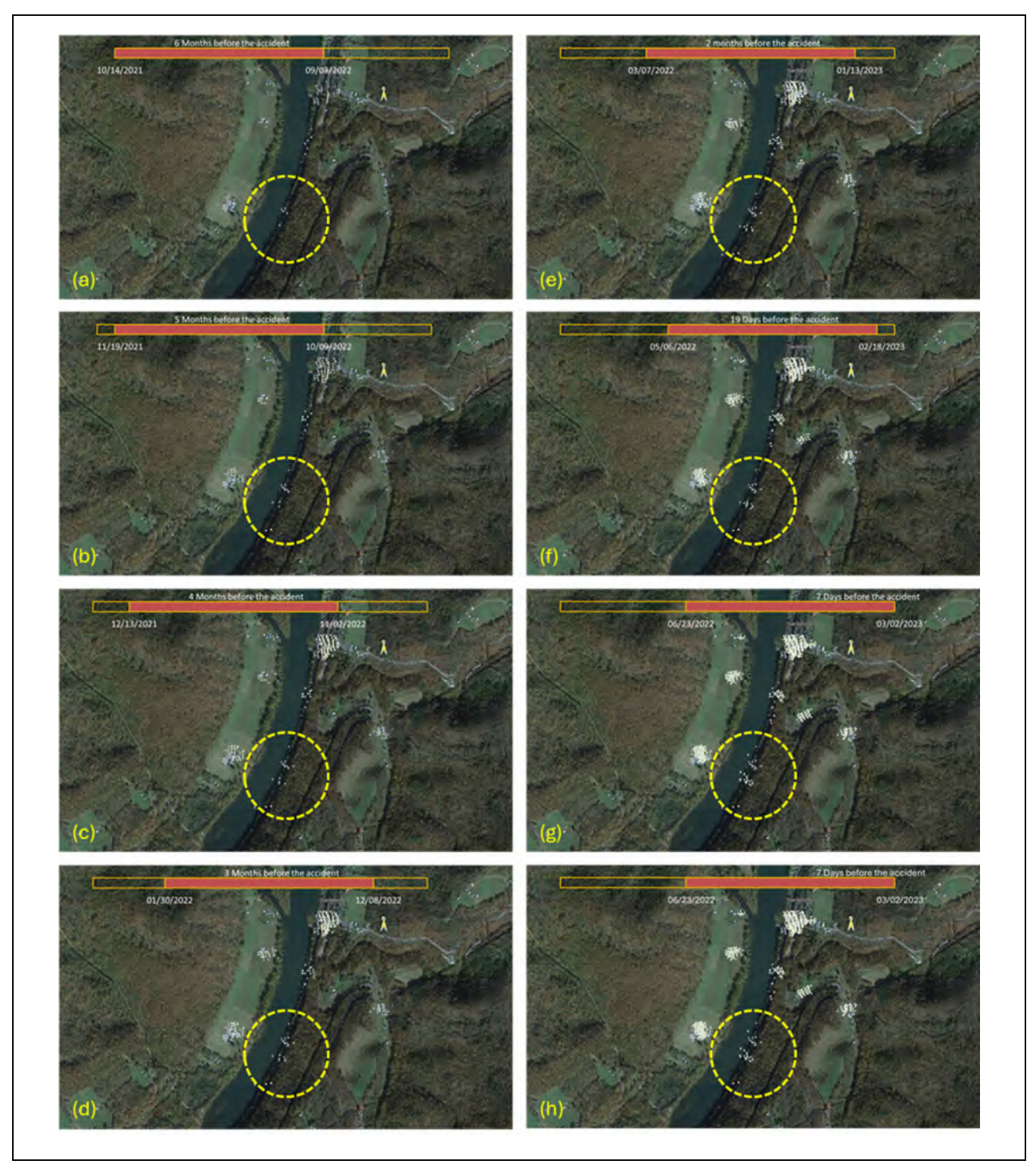


**Figure 14.** Validation study—DS accumulation at: (a) 6 months; (b) 5 months; (c) 4 months; (d) 3 months; (e) 2 months; (f) 1 month; (g) 19 days; and (h) 7 days before the rockfall event and derailment.

Note: DS = distributed scatterers.



**Figure 15.** DS clustering and critical area identification. *Note*: DS = distributed scatterers.

The ground surface deformation is computed in all cases in the satellite LOS. Each analysis cycles three older images to be replaced by three newer images. Since the acquisitions are 12 days apart, each new analysis is separated by one month.

## Thresholding and Accumulation

SBS analysis showed coherence of 0.3, thus, the threshold limits on the displacement computed at the DS point is set to  $\pm 20 \,\mathrm{mm}$  (Table 2). The DS accumulation over the entire observation period is shown in Figure 14 at different times before the event. The location of the event is marked by the yellow dashed circle. DS points are indicated by the white dots that are scarce 7 months before the event in the area of the event, and density increases as the points accumulate over time in potentially critical areas. DS points are detected at the onset of the analysis in other areas of the region of interest. By inspection of the optical image, these DS points correspond to known scatterers, for example, buildings.

### Clustering and Critical Area Identification

The next step in the process is the identification of the critical areas through detection of clusters. The clustering is observed both through visual inspection and through the optical image subset approach discussed in [25]. In both cases the identified clusters are marked in Figure 15 by yellow and red rectangles. In these clusters, the density of the DS points increases with time. The yellow marked areas correspond to areas of known scatterers, such as the structures in the town of Sandstone (cluster A), or agricultural buildings (clusters B and C), or are detected on flat terrain away from the track and are not of immediate interest. However, clusters F and G, marked by the

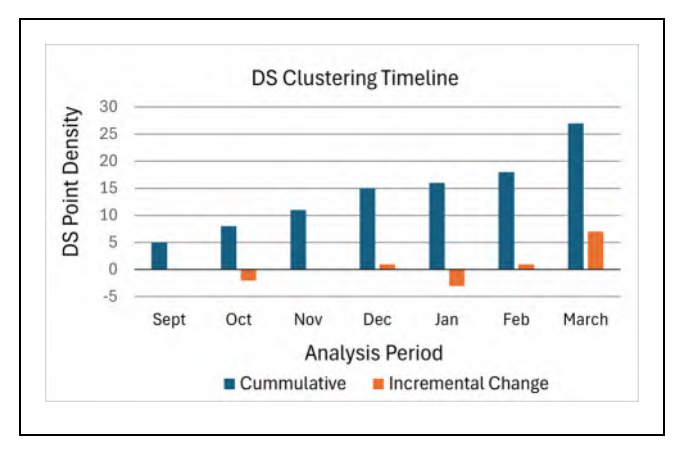


**Figure 16.** DS clustering timeline shows the DS cluster density in the critical subset and the timeline of the change. *Note*: DS = distributed scatterers.

red rectangles, are deemed the critical ones since they exhibit increasing activity over time, and are located on the path of the track on a highly sloped terrain. Cluster G is located at the derailment site and on closer investigation the two subclusters within the subset are approximately 100 m apart, which is consistent with the two distinct slope failures identified in Figure 13d. Cluster F is also identified as a critical area, however no failure occurred at the time of derailment. It was reported that following the derailment remedial action was taken on both F and G critical areas.

The DS clustering timeline analysis is shown in Figure 16. The graph shows the DS cumulative and incremental cluster density at the different times of the analysis. It is evident in both clustering and timeline analysis that the cluster has become active long before the rockfall event and derailment occurred. Furthermore, the incremental change indicates that the activity has become more pronounced about a week before the slope failure in cluster G. The activity in cluster F also raised a concern, however, the issue was addressed by the railroad before an event occurred.

#### **Conclusions**

This paper introduced the framework of a remote monitoring workflow that utilizes satellite-based radar data and other data sources for the identification and localization of critical locations along the railway ROW that exhibit higher potential to geohazard failures. The proposed approach is developed based on the MTInSAR methods, such as PSInSAR and SBAS analysis. The success of the highly accurate MTInSAR techniques depends on the detection of an adequate number of PS or DS in the region of interest for a given time period of

observation. However, as the time period of the analysis increases, seasonal vegetation coverage and errors because of larger satellite spatial baseline make the detection of both PS and DS scarce because of the loss of continuity in the observable scatterers. The proposed approach implements MTInSAR techniques using an RS concept to detect the presence of scatterers over longer time periods. In conjunction with three postprocessing that Thresholding, operations, is, Scatterer Accumulation, and Clustering Timeline, the proposed approach identifies critical locations in a very large region of the railway ROW that show much higher tendency for geohazard failure initiation, as compared with their adjacent areas. The development of the guide is achieved through investigations of sites with a history of geohazard events. A site classification guide is developed based on the parameters that affect the quality of the satellite-based C-band radar signals, and a classification chart is introduced.

The details of the development of the RS concept and the three proposed postprocessing operations, that is, Thresholding, Scatterer Accumulation, and Clustering Timeline, are discussed. Two case studies are presented to demonstrate the implementation and to validate the proposed approach. It is concluded that the RS approach in conjunction with the Thresholding, Scatterer Accumulation, and Clustering Timeline successfully detects the presence of reasonable number of scatterers at least for part of the observation period. This allows the last step of the Clustering Timeline to successfully identify the critical locations that are prone to geohazard failure, and, in most cases, detects the level of criticality through the timeline analysis.

The proposed technique has also been successfully implemented to monitor pertinent sites for track settlement. Although several areas along the tracks of the study sites showed track and embankment settlements over 30 mm in a period of a year, not all of the associated events could be conclusively attributed to the settlements.

Current and future work focuses on further enhancing the site classification guide by adding soil type and soil moisture information. To this end, additional sites will be considered, as they become available. The additional sites will also serve to further validate and qualify the proposed techniques. At present, a soil moisture change model based on coherence measurements is introduced that shows great promise in sites classified as A. It is expected that incorporating the effects of vegetation, the classification guide will also capture time varying site conditions. In parallel activities, current work focuses on fully automating the workflow and in particular the workflow of the preprocessing phase for data preparation and the postprocessing phase for critical area identification in active network monitoring operations where

the location of the event is not known, as well as communicating findings with the railroad operators in real time.

#### **Acknowledgments**

The authors would also like to acknowledge the assistance provided by CSX and BNSF in identifying the study sites and providing information about the events.

#### **Author Contributions**

The authors confirm contribution to the paper as follows: study conception and design: D.C. Rizos; data collection: S.V. Byrraju; analysis and interpretation of results: S.V. Byrraju, D.C. Rizos, M.A. Sutton, N. Li; draft manuscript preparation: D.C. Rizos. All authors reviewed the results and approved the final version of the manuscript.

## **Declaration of Conflicting Interests**

The authors declared no potential conflicts of interest with respect to the research, authorship, and/or publication of this article.

#### **Funding**

The authors disclosed receipt of the following financial support for the research, authorship, and/or publication of this article: This work has been funded primarily by the Federal Railroad Administration under contract 693JJ621C000013. Supplementary funding was provided by U.S. DOT University Transportation Center Program under contract 69A3552348340.

#### **ORCID iDs**

Dimitris C. Rizos https://orcid.org/0000-0001-5764-7911 Sumanth Varma Byrraju https://orcid.org/0000-0002-5633-9746

Michael A. Sutton (b) https://orcid.org/0000-0002-6946-5047

#### References

- 1. Vickerman, R. Can High-Speed Rail Have a Transformative Effect on the Economy? *Transport Policy*, Vol. 62, 2018, pp. 31–37.
- Pu, H., J. Xie, P. Schonfeld, T. Song, W. Li, J. Wang, and J. Hu. Railway Alignment Optimization in Mountainous Regions Considering Spatial Geological Hazards: A Sustainable Safety Perspective. Sustainability, Vol. 13, 2021, p. 1661.
- 3. British Geological Survey. Shallow Geohazards https://www.bgs.ac.uk/geology-projects/shallow-geohazards/.
- Hu, X., R. Bürgmann, W. H. Schulz, and E. J. Fielding. Four-Dimensional Surface Motions of the Slumgullion Landslide and Quantification of Hydrometeorological Forcing. *Nature Communications*, Vol. 11, 2020, p. 2792.

- Wang, W.-d., J. Li, and Z. Han. Comprehensive Assessment of Geological Hazard Safety Along Railway Engineering Using a Novel Method: A Case Study of the Sichuan-Tibet Railway, China. *Geomatics, Natural Hazards and Risk*, Vol. 11, 2020, pp. 1–21.
- Anderson, M. G., T. Glade, and M. J. Crozier. *Landslide Hazard and Risk*. John Wiley and Sons Ltd, Hoboken, NJ, 2005.
- Petley, D. N. Global Patterns of Loss of Life From Landslides. *Geology*, Vol. 40, No.10, 2012, pp. 927–930.
- 8. Froude, M. J., and D. N. Petley. Global Fatal Landslide Occurrence from 2004 to 2016. *Natural Hazards and Earth System Sciences*, Vol. 18, No. 8, 2018, pp. 2161–2181.
- Tsai, T. L., H. E. Chen, and J. C. Yang. Numerical Modeling of Rainstorm-Induced Shallow Landslides in Saturated and Unsaturated Soils. *Environmental Geology*, Vol. 58, 2008, pp. 1269–1277.
- Beyabanaki, A. R. S., A. C. Bagtzoglou, and E. N. Anagnostou. Effects of Groundwater Table Position, Soil Strength Properties and Rainfall on Instability of Earthquake-Triggered Landslides. *Environmental Earth Sciences*, Vol. 75, 2016, pp. 1–13.
- Handwerger, A. L., E. J. Fielding, M. H. Huang, G. L. Bennett, C. Liang, and W. H. Schulz. Widespread Initiation, Reactivation, and Acceleration of Landslides in the Northern California Coast Ranges due to Extreme Rainfall. *Journal of Geophysical Research: Earth Surface*, Vol. 124, No. 7, 2019, pp. 1782–1797.
- 12. European Space Agency. Railway Infrastructure Monitoring. February 23, 2023. https://space4rail.esa.int/projects/theme/railway-infrastructure-monitoring.
- Chang, L., R. P. Dollevoet, and R. F. Hanssen. Nation-wide Railway Monitoring Using Satellite SAR Interferometry. *IEEE Journal of Selected Topics in Applied Earth Observations and Remote Sensing*, Vol. 10, 2016, pp. 596–604.
- Xu, X., D. T. Sandwell, and B. Smith-Konter. Coseismic Displacements and Surface Fractures from Sentinel-1 InSAR: 2019 Ridgecrest Earthquakes. Seismological Research Letters, Vol. 91, 2020, pp. 1979–1985.
- Hooper, A., H. Zebker, P. Segall, and B. Kampes. A New Method for Measuring Deformation on Volcanoes and Other Natural Terrains Using InSAR Persistent Scatterers. Geophysical Research Letters, Vol. 31, 2004. https://doi. org/10.1029/2004GL021737.
- Liu, Z., H. Qiu, Y. Zhu, Y. Liu, D. Yang, S. Ma, J. Zhang, Y. Wang, L. Wang, and B. Tang. Efficient Identification and Monitoring of Landslides by Time-Series InSAR Combining Single-and Multi-Look Phases. *Remote Sensing*, Vol. 14, 2022, p. 1026.
- Dai, K., Q. Xu, Z. Li, R. Tomas, X. Fan, X. Dong, W. Li,
   Z. Zhou, J. Gou, and P. Ran. Post-Disaster Assessment of
   2017 Catastrophic Xinmo Landslide (China) by Space-borne SAR Interferometry. *Landslides*, Vol. 16, 2019,
   pp. 1189–1199.
- Dong, J., L. Zhang, M. Tang, M. Liao, Q. Xu, J. Gong, and M. Ao. Mapping Landslide Surface Displacements with Time Series SAR Interferometry by Combining Persistent and Distributed Scatterers: A Case Study of Jiaju

- Landslide in Danba, China. Remote Sensing of Environment, Vol. 205, 2018, pp. 180–198.
- 19. Hu, B., J. Chen, and X. Zhang. Monitoring the Land Subsidence Area in a Coastal Urban Area with InSAR and GNSS. *Sensors*, Vol. 19, 2019, p. 3181.
- Singhroy, V. SAR Integrated Techniques for Geohazard Assessment. Advances in Space Research, Vol. 15, 1995, pp. 67–78.
- Byrraju, S. V., D. Rizos, M. Sutton, and N. Li. Enhancing Railway Safety Through Satellite-Based Monitoring for Rockfall Potential. *Proc.*, ASME/IEEE Joint Rail Conference, Columbia, South Carolina, May 13–15, 2024
- 22. Byrraju, S. V., D. Rizos, M. Sutton, N. Li, and K. Hughes. On the Use of InSAR Techniques to Detect Precursors of Shallow Geohazards in Railway Right of Way. *Proc.*, *AREMA Annual Meeting*, Indianapolis, IN, 2023.
- Li, N., D. C. Rizos, and M. Z. Sutton. Development of Coherence-Soil Moisture Models for Prediction of Railway Infrastructure Failure. *Remote Sensing*, 2025, p. (In Prepartion).
- 24. OSHA. 1926 Subpart P App A Soil Classification. February 18, 2020. https://www.osha.gov/laws-regs/regulations/standardnumber/1926/1926SubpartPAppA.
- Byrraju, S. Satellite Radar Imagery for Ground Hazard Risk Monitoring in Railway Tracks and Slopes. PhD dissertation, University of South Carolina, Columbia, SC, 2025.
- Ferretti, A., C. Prati, and F. Rocca. Permanent Scatterers in SAR Interferometry. *IEEE Transactions on Geoscience* and Remote Sensing, Vol. 39, No. 1, 2001, pp. 8–20.
- Hooper, A. J. Persistent Scatterer Radar Interferometry for Crustal Deformation Studies and Modeling of Volcanic Deformation. PhD Dissertation, Stanford University, Palo Alto, CA, 2006.
- Ferretti, A. Satellite InSAR Data Reservoir Monitoring from Space. EAGE Publications, Bunnik, Netherlands, 2014.
- Damien, C., and M. Nada. InSAR Coherence and Intensity Changes Detection. 2017. DOI: 10.5772/65779
- Fiaschi, S., E. P. Holohan, M. Sheehy, and M. Floris. PS-InSAR Analysis of Sentinel-1 Data for Detecting Ground Motion in Temperate Oceanic Climate Zones: A Case Study in the Republic of Ireland. *Remote Sensing*, Vol. 11, 2019, p. 348.
- 31. Bamler, R., and D. Just. Phase Statistics and Decorrelation in SAR Interferograms. *Proc., Proceedings of IGARSS'93-IEEE International Geoscience and Remote Sensing Symposium*, Tokyo, Japan, 1993, IEEE, New York, pp. 980–984.
- 32. Asrar, G., and D. J. Dokken. 1993 Earth Observing System Reference Handbook. 1993. https://ntrs.nasa.gov/citations/ 19930014548
- 33. Roberto, C., A. Jailson, M. Hanna, P. Julia, and R. A. Wilson. Applicability of the InSAR Technique for Slope Monitoring. *Soils and Rocks*, Vol. 46, No. 4, 2023, p. 11.
- Flores-Anderson, A. I., K. Herndon, R. B. Thapa, and E. A. Cherrington. The SAR Handbook: Comprehensive Methodologies for Forest Monitoring and Biomass Estimation. 2019. https://earthdata.nasa.gov/s3fs-public/2025-04/

- SARHB\_FullRes\_2019.pdf?VersionId = XU9mWLgLcP-tEZiL3.m72A2L8lcJOxub4
- Desmond, P., Y. James, E. Jerry, R. Karen, C. Scott, and H. Roger. *InSAR Applications for Highway Transportation Projects*. 2006. https://rosap.ntl.bts.gov/view/dot/42936/ dot 42936 DS1.pdf
- 36. Esch, S. Determination of Soil Moisture and Vegetation Parameters from Spaceborne C-Band Sar on Agricultural Areas. PhD thesis, Universität zu Köln, 2018.
- 37. Marzahn, P., and R. Ludwig. On the Derivation of Soil Surface Roughness from Multi Parametric PolSAR Data and its Potential for Hydrological Modeling. *Hydrology and Earth System Sciences*, Vol. 13, 2009, pp. 381–394.
- 38. Gaber, A., F. Soliman, M. Koch, and F. El-baz. Using Full-Polarimetric SAR Data to Characterize the Surface Sediments in Desert Areas: A Case Study in El-Gallaba Plain, Egypt. *Remote Sensing of Environment*, Vol. 162, 2015, pp. 11–28.
- Jack, H. Manufacturing Processes. Surface, 2013. http://engineeronadisk.com/V3/engineeronadisk-67.html.
- Prakash, R., and D. Singh. Modeling of Scattering Response for Retrieval of Soil Parameters with Bistatic Radar. *Mathematics Applied in Information Systems*, Vol. 2, 2018, pp. 168–196.
- 41. Yang, H. W., B. Baudet, and T. Yao. Characterization of the Surface Roughness of Sand Particles Using an Advanced Fractal Approach. *Proceedings of the Royal Society A: Mathematical, Physical and Engineering Sciences*, Vol. 472, 2016, p. 20160524.
- Li, L., M. A. Nearing, M. H. Nichols, V. O. Polyakov, C. L. Winter, and M. L. Cavanauggh. Temporal and Spatial Evolution of Soil Surface Roughness on Stony Plots. *Soil and Tillage Research*, Vol. 200, 2020, p. 104526.
- 43. Sabrina, E. Determination of Soil Moisture and Vegetation Parameters from Spaceborne C-Band SAR on Agricultural Areas 2018. https://d-nb.info/1153543524/34
- 44. Nolan, M., and D. R. Fatland. Penetration Depth as a DInSAR Observable and Proxy for Soil Moisture. *IEEE*

- Transactions on Geoscience and Remote Sensing, Vol. 41, 2003, pp. 532–537.
- 45. Barrett, B., P. Whelan, and E. Dwyer. The Use of C-and L-band Repeat-Pass Interferometric SAR Coherence for Soil Moisture Change Detection in Vegetated Areas. *Open Remote Sensing Journal*, Vol. 5, 2012, pp. 37–53.
- Bourgeau-Chavez, L. L., Y. M. Lee, M. Battaglia, S. L. Endres, Z. M. Laubach, and K. Scarbrough. Identification of Woodland Vernal Pools with Seasonal Change PAL-SAR Data for Habitat Conservation. *Remote Sensing*, Vol. 8, 2016, p. 490.
- 47. Evans, T. L., M. Costa, W. Tomas, and A. R. Camilo. A SAR Fine and Medium Spatial Resolution Approach for Mapping the Brazilian Pantanal. *Geografia*, Vol. 38, 2013, pp. 25–43.
- 48. ESA. Copernicus Open Access Hub. April 28, 2023. https://scihub.copernicus.eu/.
- 49. ASF. Alaska Satellite Facility Distributed Active Archive Center. April 5, 2023. https://search.asf.alaska.edu/#/.
- 50. The Weather Company. October 4, 2024. www.wunder-ground.com.
- 51. United States Department of Agriculture Natural Resources Conservation Service. SSURGO Data Packaging and Use. 2012. https://www.nrcs.usda.gov/sites/default/files/2022-08/SSURGO-Data-Packaging-and-Use-6.pdf
- National Centers for Environmental Information. USCRN Intrumtents. 2023. https://www.ncei.noaa. gov/access/crn/instruments.html. Accessed July 1, 2024.
- U.S. Department of Agriculture. Soil Survey Geographic (SSURGO) Database for Wasco County, Oregon, Northern Part. U.S. Department of Agriculture, Natural Resources Conservation Service, Fort Worth, TX, 2022.

The opinions expressed in this article are solely those of the authors and do not represent the opinions of the funding agencies.